

# In-situ PLL-g-PEG Functionalized Nanopore for Enhancing Protein Characterization

Mostafa Salehrozveh,<sup>[b, d]</sup> Anne-Kathrine Kure Larsen,<sup>[a, f, g]</sup> Milos Stojmenovic,<sup>[c]</sup> Federico Thei,<sup>\*,[d]</sup> and Mingdong Dong<sup>\*,[a, e]</sup>

**Abstract:** Single-molecule nanopore detection technology has revolutionized proteomics research by enabling highly sensitive and label-free detection of individual proteins. Herein, we designed a small, portable, and leak-free flowcell made of PMMA for nanopore experiments. In addition, we developed an *in situ* functionalizing PLL-g-PEG approach to produce non-sticky nanopores for measuring the volume of diseases-relevant biomarker, such as the Alpha-1 antitrypsin (AAT) protein. The *in situ* functionalization method allows continuous monitoring, ensuring adequate functionalization, which can be directly used for translocation experiments. The functionalized nanopores exhibit improved

characteristics, including an increased nanopore lifetime and enhanced translocation events of the AAT proteins. Furthermore, we demonstrated the reduction in the translocation event's dwell time, along with an increase in current blockade amplitudes and translocation numbers under different voltage stimuli. The study also successfully measures the single AAT protein volume (253 nm<sup>3</sup>), which closely aligns with the previously reported hydrodynamic volume. The real-time *in situ* PLL-g-PEG functionalizing method and the developed nanopore flowcell hold great promise for various nanopores applications involving non-sticky single-molecule characterization.

## Introduction

Recent scientific interest in nanopore-based detection has been sparked by its ability to detect nano-sized particles and biomolecules such as nucleic acids,<sup>[1-5]</sup> proteins,<sup>[6-8]</sup> and complexes<sup>[9-11]</sup> in media without labelling. The presence of a nanopore in an electrically insulating membrane can serve as a single-entity detector. Nanopores can be either formed by a biological channel in high electrical resistance lipid bilayers, solid-state substrate, and hybrids of both membranes,<sup>[11,12]</sup> or they can be drilled as a hole in synthetic materials such as silicon, graphene, or polymers.<sup>[13,14]</sup> By developing solid-state nanopores, the translocations of proteins, nucleic acids, and small molecules can be studied.<sup>[15-17]</sup> Nanopore analysis is a simple approach by inferring information about a molecule's size, shape, charge, and dipole based on the ionic current blockage results from molecules passing through a nanopore.<sup>[18]</sup> An ionic current is monitored through the nanopore by

applying a voltage across the membrane. Biomolecule like DNA or proteins translocations through the nanopore affects the current level, which leads to a translocation event signal.<sup>[18,19]</sup>

In light of the advances in nanopore protein detection, many studies have been done that improve the sensing performance of solid-state nanopores due to their robustness and stability under tough conditions (such as temperature,<sup>[21]</sup> pH<sup>[22]</sup>), as well as the ability to integrate them into embedded systems and electronics.<sup>[23]</sup> For instance, the translocation of more than a million-protein using modified solid-state nanopores and a method for restoring clogged pores in real-time were investigated by Jugal Saharia et al.<sup>[24]</sup> In the other study, Matthew O'Donohue et al. were able to distinguish the transferrin protein and its receptor populations by solid-state nanopores.<sup>[25]</sup> Also, a solid-state nanopore was used to quantify the aggregation of different proteins based on their non-uniform charge distribution by Mitu C. Acharjee et al.<sup>[26]</sup>

[a] A.-K. Kure Larsen, Prof. M. Dong  
 Interdisciplinary Nanoscience Center (iNANO)  
 Aarhus University  
 Aarhus (Denmark)  
 E-mail: dong@inano.au.dk

[b] Dr. M. Salehrozveh  
 Department Of Physics And Astronomy  
 University of Bologna  
 Bologna (Italy)


[c] Dr. M. Stojmenovic  
 Computer Science  
 Singidunum university  
 Belgrade (Serbia)


[d] Dr. M. Salehrozveh, Dr. F. Thei  
 Elements srl  
 Cesena (Italy)  
 E-mail: fthei@elements-ic.com

[e] Prof. M. Dong  
 Department of Biology - Center for Electromicrobiology  
 Aarhus University  
 Aarhus (Denmark)

[f] A.-K. Kure Larsen  
 Sino-Danish Center for Education and Research  
 Aarhus (Denmark)

[g] A.-K. Kure Larsen  
 University of the Chinese Academy of Sciences  
 Beijing (China)

 Supporting information for this article is available on the WWW under <https://doi.org/10.1002/asia.202300515>

 © 2023 The Authors. Chemistry - An Asian Journal published by Wiley-VCH GmbH. This is an open access article under the terms of the Creative Commons Attribution Non-Commercial NoDerivs License, which permits use and distribution in any medium, provided the original work is properly cited, the use is non-commercial and no modifications or adaptations are made.

Blood components such as Alpha-1 antitrypsin (AAT) play a critical role in preventing tissue breakdown by proteolytic enzymes. It protects the lungs from neutrophil elastase, an enzyme responsible for degrading elastin.<sup>[27,28]</sup> It has been found that serum levels of AAT protein increase in some virulent diseases.<sup>[29,30]</sup> In addition to being recognized as a biomarker for Alzheimer's disease,<sup>[31]</sup> AAT serum levels are elevated in several inflammatory diseases and malignancies, including lung cancer,<sup>[32,33]</sup> gastrointestinal cancer,<sup>[34]</sup> and pancreatic cancer.<sup>[35]</sup> AAT mutations cause polymerization induced Serpinopathies and accelerated aggregation.<sup>[36]</sup> The Alpha 1-Antitrypsin deficiency (AATD) pathogenesis of liver disease is caused by alpha-1 antitrypsin polymers, which are aggregates of misfolded proteins associated with hepatocellular carcinoma, hepatocellular injury, and liver fibrosis.<sup>[37]</sup> A deletion in certain variant of Cystic Fibrosis (CF) transmembrane regulator (CFTR) that triggers CF, or AATD missense mutations that cause liver disease, lung cancer, and misfolding and/or aggregate formation.<sup>[38]</sup> Most polymers remain inside hepatocytes, some are excreted into the bloodstream. In order to determine the properties of unfolded and disordered proteins, chain size, shape, and polymer scaling can all be considered.<sup>[39]</sup> Considering that aggregated proteins would have greater volume than singly folded proteins, solid state nanopores can be used to characterize and estimate the volume of AAT proteins. However, they have been hampered by difficulties like analytes adhering to the sidewall nanopore, which may cause irreversible clogging issues during protein detection.<sup>[40-43]</sup> The solution to these problems lies in a variety of strategies that have been reported for functionalizing solid-state nanopores, including the deposition of metals<sup>[44]</sup> and oxides<sup>[45,46]</sup> to produce nanopore structures.<sup>[47-49]</sup> Functionalizing the solid-state nanopore surface can prevent the target biomolecule from sticking to nanopore sidewalls. It has been reported that several existing chemicals acted effectively at inhibiting nonspecific adsorption on SiN surfaces, such as 3-(aminopropyl) trimethoxysilane (APTMS),<sup>[50,51]</sup> polyethylene glycol (PEG),<sup>[52-54]</sup> and molecular weight modified ethylene glycol chains.<sup>[55]</sup> Moreover, ex-situ polyacrylamide-based polymer surface functionalizing has been shown to prevent protein interactions with solid-state nanopores.<sup>[56]</sup> In addition, apart from focused ion beam and focused electron beam imaging to visualize the morphology of the nanopore functionalizing layer structure, which are expensive and time-consuming methods, a controllable molecular functionalizing that approaches the nanometer scale is mandatory for reducing protein adsorption. It has been shown that *in situ* layer-by-layer deposition of poly(L-lysine) (PLL) and PLL-g-PEG-biotin modulates the ionic selectivity of a conical nanopore and can be used to design biosensors.<sup>[57]</sup> However, due to the electrostatic interaction of the positive PLL backbone with silicon nitride nanopore (negatively charged), PEG chains could float in the nanopore, reducing surface protein adsorptions.<sup>[54,58-61]</sup>

In this work, we designed and fabricated miniaturized Poly (methyl methacrylate) (PMMA) nanopore flowcell as shown in Figure 1(A, B). Then, we measured SiN nanopore conductance at different concentrations of Phosphate-buffered saline (PBS), nanopore size, ion current rectification, and noise level at

different voltages. Furthermore, we proposed an *in situ* approach to functionalize the SiN nanopore by PLL-g-PEG at physiological pH to minimize sticking nanopore behavior. Also, the noise level of non-functionalized and PLL-g-PEG functionalized nanopores were compared. In addition to the decrease in the diameter of the nanopore, improvements in the lifetime, storage capacity, and reusability of the nanopore were also demonstrated. We used functionalized nanopore to facilitate detecting, counting, and estimating the AAT protein volume in fluids, which can serve as a biomarker for a wide range of diseases and cancers. The PLL-g-PEG chains drive to nanopore by applying voltage and allowing them to adhere to sidewall nanopore electrostatically. As opposed to the ex-situ, by *in situ* functionalization method, the PLL-g-PEG thickness could be monitored. Figure 1(D) shows the chemical structure of a (PLL-g-PEG) copolymer as well as the functionalization of a flat glass surface to estimate the PLL-g-PEG thickness by atomic force microscopy (AFM).

## Results and Discussion

The conductivity measurements, PLL-g-PEG functionalization, and protein translocation were investigated, after chlorinating the reference electrodes of our proprietary nanopore flowcell by 50% NaOCl for 2 minutes, as shown in Figure 1(B). In order to remove contaminants and activate the surfaces, Piranha pretreatment and wetting by mixing IPA and water was used before the functionalizing step.

Figure 2 presents I-V curves and conductance of a non-functionalized 20 nm SiN nanopore in 0.125×PBS, 0.25×PBS, 0.5×PBS, and 1.0×PBS solutions at physiological pH. According to the cylindrical model, the open-pore conductance (G) is calculated as follows:<sup>[62,63]</sup>

$$G = s \left( \frac{4L}{\pi d^2} + \frac{1}{d} \right)^{-1} \quad (1)$$

$$d = \frac{G}{2s} \left( 1 + \sqrt{1 + \frac{16sL}{\pi G}} \right) \quad (2)$$

In equation 1, S represents the solution conductivity, and L represents the membrane thickness. A 20 nm pore with 30 nm thickness showed a conductance of 9.8 nS in 1.0×PBS. Based on equation 2 and the calculated nanopore conductance from equation 1, the 18.7 nm diameter of the nanopore is achieved, which is close to the actual values.

Moreover, when the PBS concentration is relatively low, the I-V curve is not linear, and lower conductivity in the positive voltages can be seen in Figure 2(A) (the inset represents the I-V curve of 0.125×PBS). This non-linear I-V curve is renowned as ionic current rectification (ICR), which can be observed in different current levels at the same voltage with different polarity. A precise theoretical knowledge of this nonlinear phenomena plays a key role in designing and fabricating nanopores for different applications.<sup>[64]</sup> In summary, on the tip

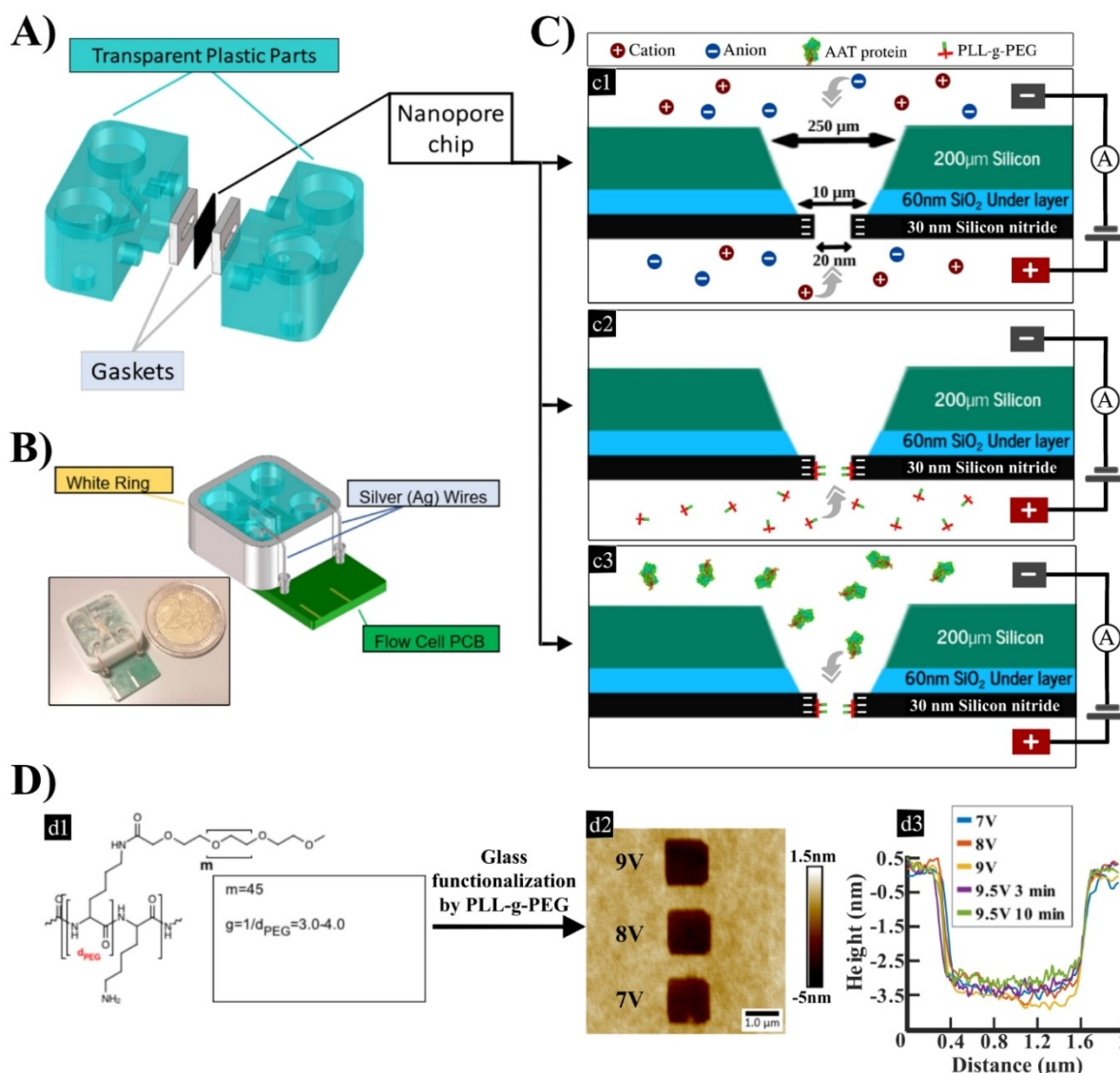


**Figure 1.** (A) The schematic of the nanopore flowcell pieces, and (B) the assembled nanopore flowcell, the inset image displays the real size of the nanopore flowcell compared to a coin. The nanopore fluidic setup and its structure, consisting of thicknesses of 200  $\mu\text{m}$  Silicon, 60 nm  $\text{SiO}_2$ , and 30 nm  $\text{SiN}$  layers is shown in (C) and the non-functionalized 20 nm  $\text{SiN}$  nanopore (c1), *in situ* PLL-g-PEG functionalization (c2), and protein translocation (c3) are depicted. The PLL-g-PEG chemical structure and thickness measurement on a flat glass coverslip are seen in (D), along with the PLL-g-PEG chemical structure (d1),<sup>[20]</sup> an AFM topography image of a lithography area on glass functionalized with PLL-g-PEG (d2), and profiles of representative lithography scraped areas (d3) are presented.

of the nanopore, positively charged ions form, followed by a group of counter-charged ions known as the electric double layer (EDL). Meanwhile, the majority of negative ions (anions) remain near the nanopore's core. Thus, at low values of the Debye length ( $\lambda_D$ ), EDL does not overlap; therefore, it does not affect ion migration. As a result, the applied potential bias drives the ions at the nanopore's core.

Conversely, by increasing the  $\lambda_D$ , resistive forces arise at the nanopore's tip, dampening the ionic current.<sup>[65,66]</sup> Compared to long nanopores, short nanopores have considerable advantages, including a higher ionic permeation coefficients and increased biosensor sensitivity.<sup>[67]</sup> In order to improve energy conversion, desalination, and biosensor sensitivity, it is essential to achieve significant ICR in nanopores. The ICR ratio is

generally defined as the ratio of forward and backward ionic current for equivalent potential biases. Based on recent research, most rectifying nanopores have a length of  $\geq 500$  nm,<sup>[68]</sup> but this event was rarely observed in nanopores with less than 200 nm length.<sup>[63]</sup> For instance, a nanopore prepared from  $\text{SiO}_2$  pyramidal membranes with 30 nm thickness had an ICR ratio of less than 2.<sup>[69]</sup> Different concentrations of KCl solutions from 1 to 1000 mM did not indicate rectification in the current by using 55 nm-long truncated pyramidal silicon nanopores.<sup>[70]</sup> Moreover, a strongly charged conical pore with a 200 nm length was simulated with an ICR ratio of 2.<sup>[71]</sup> As indicated in the inset of Figure 2A, the ICR clearly appeared at a low salt concentration of  $0.125 \times \text{PBS}$ . The ICR ratio at low salt concentrations of  $0.125 \times \text{PBS}$  is 1.25. This ICR phenomenon can

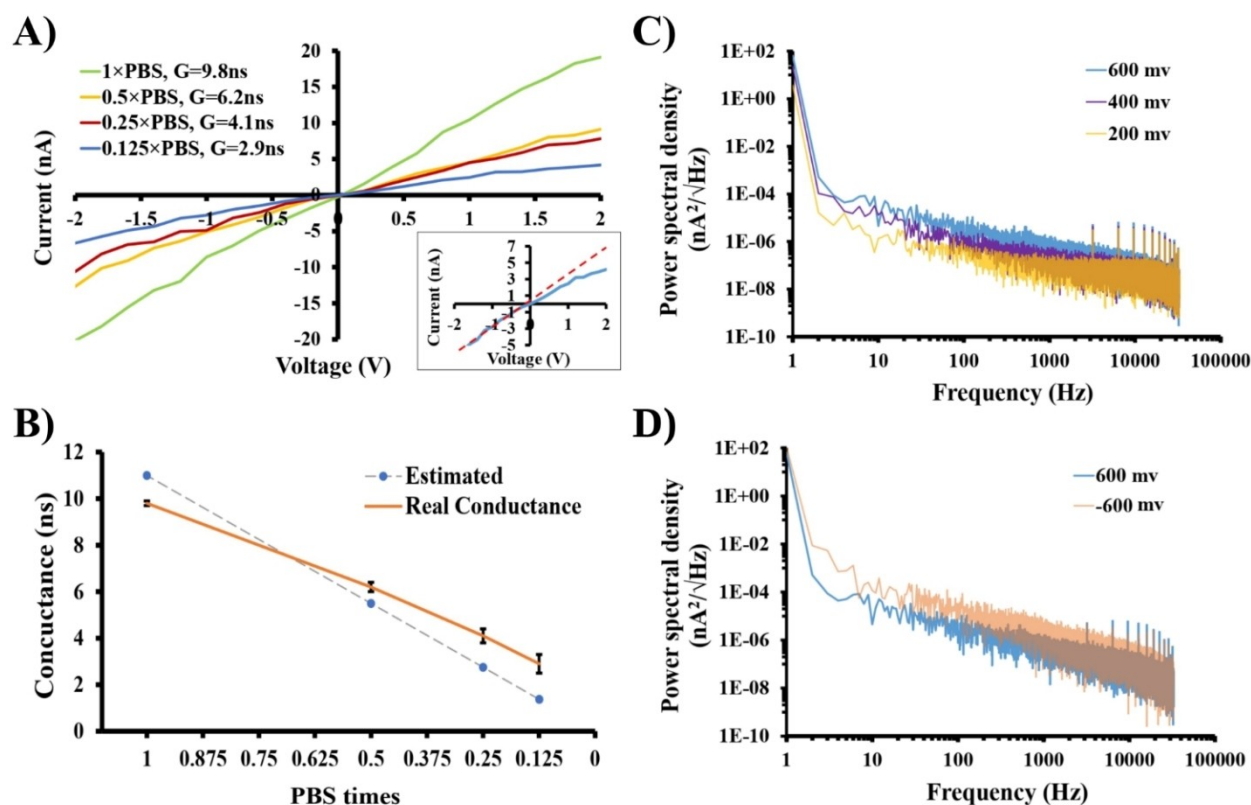


**Figure 2.** (A) I–V curves of 20 nm SiN nanopore in 0.125×PBS, 0.25×PBS, 0.5×PBS, and 1.0×PBS at physiological pH, The inset displays the ion current rectification in 0.125×PBS. (B) Comparison of estimated (dashed line) and measured (orange line) nanopore conductance at different PBS buffer concentrations. PBS time of 1 indicates PBS without dilutions, and 0.125 means eight times the dilution. (C) Current PSD at 200, 400, 600 mV stimulus voltages and (D) comparison of nanopore PSD noise at +600 and –600 mV in 1.0×PBS, pH 7.4.

be explained by decreasing electrolyte concentration causing increases in Debye length. The Debye length ( $\lambda_D$ ) in 1.0×PBS and 0.125×PBS were assumed to be approximately 0.7,<sup>[72]</sup> and 2.2 nm,<sup>[73]</sup> respectively. Anions (negative ions) tend to stay near the nanopore's core, which can lead to EDL overlapping at low electrolyte concentrations, and dampening ion migration. By lowering the salt concentration, the potential bias drives the ions to the nanopore's core, and this ion migration imitation will appear as ICR with a different polarity at the same voltage.<sup>[74,75]</sup> The EDL become thicker, and non-linear I–V curves were observed as the PBS concentration decreased.<sup>[76]</sup>

The calculated and experimental conductance in 0.125×PBS, 0.25×PBS, 0.5×PBS, and 1.0×PBS solutions at physiological pH were plotted in Figure 2B (by respect to 1.0×PBS conductivity of 1.6 s/m and equation 1). As a result, standard equations can precisely explain the trend of nanopores conductance and a slight difference between the calculated and experimental conductance value is caused by the rectification effect on the I–V curve's slope at low salt concentrations. As shown in figure 2(C), the PSD noise level of non-functionalized 20 nm SiN nanopores was raised by increasing stimulus voltage from 200 to 600 mV, especially at frequencies less than 10 kHz. Figure 2(D) shows the PSD noise versus frequency curve for 600 and –600 mV. Surprisingly, the polarity of the stimulus voltage on the nanopore base side effect the PSD noise level and the rms noise for 600 and

–600 mV, were 0.14 and 0.5 nA, respectively. The structure and shape of the nanopore may have been responsible for these differences.

AFM imaging and lithography was performed on PLL-g-PEG on a glass surface to give an indication of the layer thickness, by increasing the force (voltage) and time with which a 1  $\mu\text{m}^2$  area was scraped away with the AFM tip, until the depth reached a saturated level. As shown in figure 1(d3), the PLL-g-PEG layer is roughly around 3.5 nm when allowed to attach to a flat surface. To prevent proteins from adhering to nanopore walls, we used the *in situ* PLL-g-PEG functionalization process. As PLL-g-PEG chains flow through the nanopore by driven voltage, it was expected to see a thinner and more uniform PLL-g-PEG layer created by *in situ* method than was founded during ex-situ functionalization. Considering the ~3.5 nm length of PLL-g-PEG, it was expected that the nanopore diameter would be reduced by less than 7 nm. After ex-situ functionalizing the nanopore, there were several layers of PLL-g-PEG on the nanopore side walls (~11 nm) which was neither repeatable nor controllable. In this study, by using the *in situ* method, the 20 nm SiN nanopores were functionalized with PLL-g-PEG in a well-controlled manner. In a physiological buffer solution, positively charged PLL backbones adsorb onto negatively charged SiN surfaces<sup>[77,78]</sup> through electrostatic interactions.<sup>[52–54,79]</sup> Figure 1(c2) shows a schematic of nanopore functionalization, when 800 mV is applied to the Cis chamber,

where positively charged chains of PLL-g-PEG enter the nanopore tip and form a thin layer of PLL-g-PEG.

Real-time *in situ* 20 nm SiN nanopore functionalization is shown in Figure 3(A), including: opening the Faraday cage to inject PLL-g-PEG solution (O), 3 times PLL-g-PEG solution injecting in order to completely replace the previous buffer with PLL-g-PEG, closing the Faraday cage (C), PLL-g-PEG diffusion (related to the movement of polymer chains towards the nanopore's tip), and finally the nanopore's sidewall

functionalization. As shown in Figure 3(A), It should be noted that after 1st PLL-g-PEG injection, the current level was dropped about %15 which is probably due to the difference in the solution conductivity of Cis and trans chambers. The current level was stabilized by completing PLL-g-PEG Functionalization on the nanopore sidewalls after 50 to 70 seconds by 31.8% (3.5 nA) decreasing in the real time ionic current level, which is expected from the PLL-g-PEG layer. The I–V curves of a 20 nm solid-state nanopore chip in 1.0×PBS buffer solution are

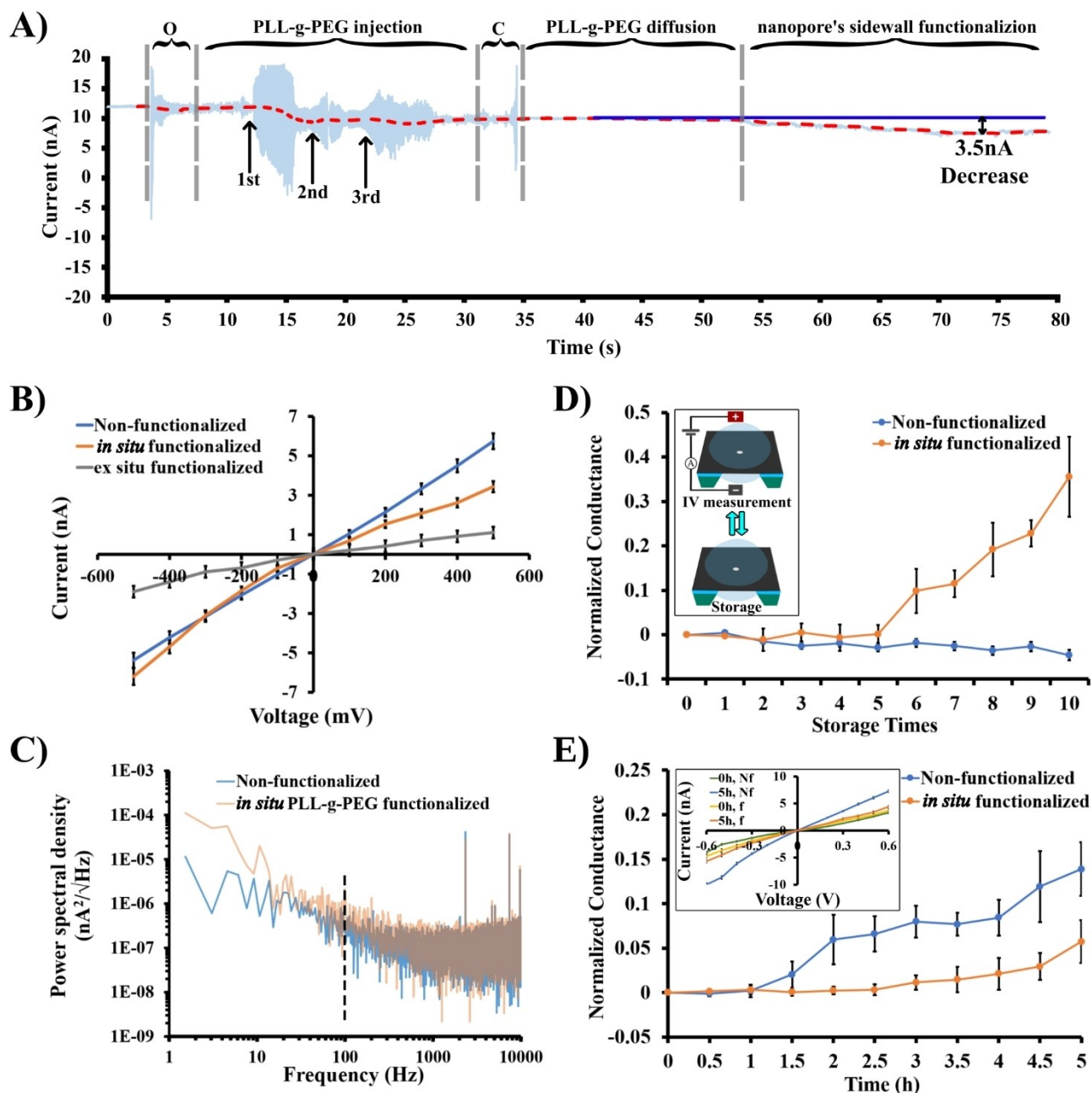


**Figure 3.** (A) Real-time ionic current trace during PLL-g-PEG functionalizing 20 nm SiN nanopore at 800 mV: open Faraday cage (o), 3 times PLL-g-PEG injection, close cage (c), PLL-g-PEG diffusion, and nanopore's sidewall functionalization. (B) The I–V curves of *in situ*, ex-situ, and non-functionalized nanopore. (C) PSD noise of non-functionalized (Blue) and PLL-g-PEG functionalized (Orange), dashed lines show the 100 Hz line. Normalized G vs. Storage times for *in situ* functionalized and non-functionalized nanopore (D), Inset displays schematic of the nanopore storage in 0.1 × PBS, and repeating conductance measurement. Normalized conductance curves of non-functionalized and *in situ* functionalized nanopore over a course of 5 hours at 600 mV stimulus voltage (E), and the inset represent their I–V curves before and after 5 hours (Nf: non-functionalized, f: *in situ* functionalized). All measurements were done in 1.0×PBS at physiological pH.

recorded to estimate the conductance of the nanopore before and after PLL-g-PEG functionalizing by *in situ* and *ex-situ* methods as shown in Figure 3(B). The nanopore conductance was reduced more than 80.7% after *ex-situ* coating. Based on AFM image analysis, and considering the PLL-g-PEG thickness of  $\sim 3.5$  nm functionalized on a flat coverslip, the maximum expected reduction in conductance of an 18.7 nm pore by PLL-g-PEG would be 55.1% (from 9.8 nS to 4.4 nS). The ionic current slopes of a linear fitting of the experimental results yielded a decrease of about 37.7% in the nanopore's conductance ( $\Delta G = 3.7$  nS), which is a sign of 2.3 nm PLL-g-PEG functionalization layer on the nanopore's sidewall. Therefore, a nanopore of diameter  $\sim 18.7$  nm SiN is estimated to become  $\sim 14.1$  nm after PLL-g-PEG functionalization. The *in situ* PLL-g-PEG functionalized thickness ( $\sim 2.3$  nm) is about one nanometer thinner than flat glass surface PLL-g-PEG functionalized as shown in Figure 1(d3) by AFM ( $\sim 3.5$  nm), and quite thinner than the *ex-situ* nanopore functionalized one ( $\sim 11$  nm) as shown in Figure 3(B). Aside from that, the charge of the nanopore's tip wall after functionalization was slightly positive due to the PLL-g-PEG chains charge,<sup>[80–82]</sup> resulting in a parabolic I–V curve. In general, the measured currents depend less on bulk ionic concentrations than would be expected from ionic conductivity. In the positively charged nanopore's tip, the flow of cations through the nanopore is limited, which lowers pore resistance, determines its ionic selectivity, and appears as the rectification of ionic current.<sup>[83,84]</sup> We can assume that the current ion rectification of about 1.7 compared to the linear I–V curve before functionalization is due to a change in charge and nanopore shape or size. The power spectral density noise for bare and PLL-g-PEG functionalized nanopores are also compared as shown in Figure 3(C). These results show that PLL-g-PEG functionalizing has increased the power spectral noise in a low-frequency domain (less than 100 Hz) which is related to the polymer's subunits adhered to nanopore side walls that lead to an increase in noise at low-frequencies. Also, the creation of nanobubbles inside the nanopore can increase the power spectral noise which is in line with the previous studies.<sup>[56,85,86]</sup> Figure 3(D) shows the normalized conductance of non-functionalized and *in situ* PLL-g-PEG functionalized 20 nm SiN nanopores over 10 times storage. As shown in Figure 3D inset, between each storage step of nanopore chips (PLL-g-PEG functionalized and non-functionalized 20 nm SiN nanopores) in PBS, IV curves were recorded. The non-functionalized nanopore conductance remained stable with a slight decrease over storage time due to the water-based buffer in contact with our SiN nanopore, which agrees with previous studies.<sup>[87]</sup> As a result of *in situ* functionalization, PLL-g-PEG layers remained stable for up to 5 times of storage in PBS (described in experimental section) and reusing. It is obvious that after six storage time, washing process, and reusing, a portion of the PLL-g-PEG layers begun to disassemble from the SiN sidewall and the nanopore conductance increased. Eventually, after ten times of storage in PBS, the nanopore conductivity reached 8.27 nS, near that of the bare nanopores (9.8 nS).

In Figure 3(E), the normalized conductance of a 20 nm non-functionalized and PLL-g-PEG functionalized nanopore is shown

over 5 hours of continuous experiment under 600 mV, at pH 7.4. The conductance of the non-functionalized nanopore was constant by the first hour, but it was raised from 9.8 to 11.16 nS after 5 hours, due to an alteration in structure and chemistry around the nanopore's edge.<sup>[88]</sup> In contrast, the PLL-g-PEG layer on the nanopore sidewall was stable for  $\sim 4$  hours which was prevented the changing or expanding of the SiN nanopore structure under high stimulus voltage. In the other words, the lifetime of nanopore was enhanced by using PLL-g-PEG layers.

A control experiment using  $\sim 16.5$  nm non-functionalized pores was conducted by injecting 25 nM AAT protein into Cis chamber in  $1.0 \times$  PBS at physiological pH by applying 600 mV stimulus voltage. Occasionally, the non functionalized nanopore becomes irreversibly jammed after adding proteins, and only a few proteins were translocated by sticking to the sidewalls as shown in Figure 4(A). The  $\sim 16.2$  nm nanopore were used to functionalize with PLL-g-PEG for 5 minutes to be sure to fully functionalize the side walls of the nanopores, with  $\sim 9.5$  nm final estimated pore size after PLL-g-PEG functionalizing was used to test the unsticking behavior of the PLL-g-PEG nanopores. The same AAT protein concentration was injected to the Cis chamber using the same experimental environment and conditions, and we observed about 15 events/s translocation through the functionalized nanopores as shown in Figure 4(B), which is 15 times more than that through non-functionalized nanopore as shown in Figure 4(C) translocation histogram. AAT protein translocations through non-functionalized nanopores takes about 105 times longer than through PLL-g-PEG functionalized nanopores (with mean dwell time about 0.4 ms) as depicted in the scatter plot in Figure 4(C). In addition, we observed increasing of translocation events amplitude about 25% (from 0.24 to 0.3 nA) due to smaller nanopore diameter after PLL-g-PEG functionalization which led to higher translocation events amplitude for the same protein translocation. This change is roughly close to the nanopore volume changes before and after functionalization with PLL-g-PEG. The vast number of translocations observed without pore-clogging and/or sticking behavior indicates that a PLL-g-PEG functionalized pore is ideal for AAT protein translocations. The Single PLL-g-PEG layer effectively prevents the protein from continuous interactions with sidewall nanopores, as shown in this study.

Figures 4(D and E) show current traces for 500 nM AAT protein translocation through  $\sim 9.5$  nm functionalized nanopores in different voltages (200, 400, and 600 mV) using  $1.0 \times$  PBS at physiological pH. Figure 4(F) shows the scatter plots of 500 nM AAT protein translocation events under different voltages together with their dwell time and amplitude distribution. As illustrated in the scatter plots in Figure 4(F), the Gaussian distribution fitted curve on histogram data and inset plots indicates that by increasing the voltage from 200 mV to 400 and then 600 mV, the dwell time decreased from  $3.6 \pm 1.6$  ms to  $1 \pm 0.5$  and  $0.473 \pm 0.3$  ms, respectively. On the other hand, increasing the voltage led to an increase in the current blockade's amplitude from  $0.09 \pm 0.06$  nA to  $0.18 \pm 0.09$  and  $0.28 \pm 0.08$  nA for 200, 400, and 600 mV stimulus voltage respectively. The AAT protein translocation event's frequency

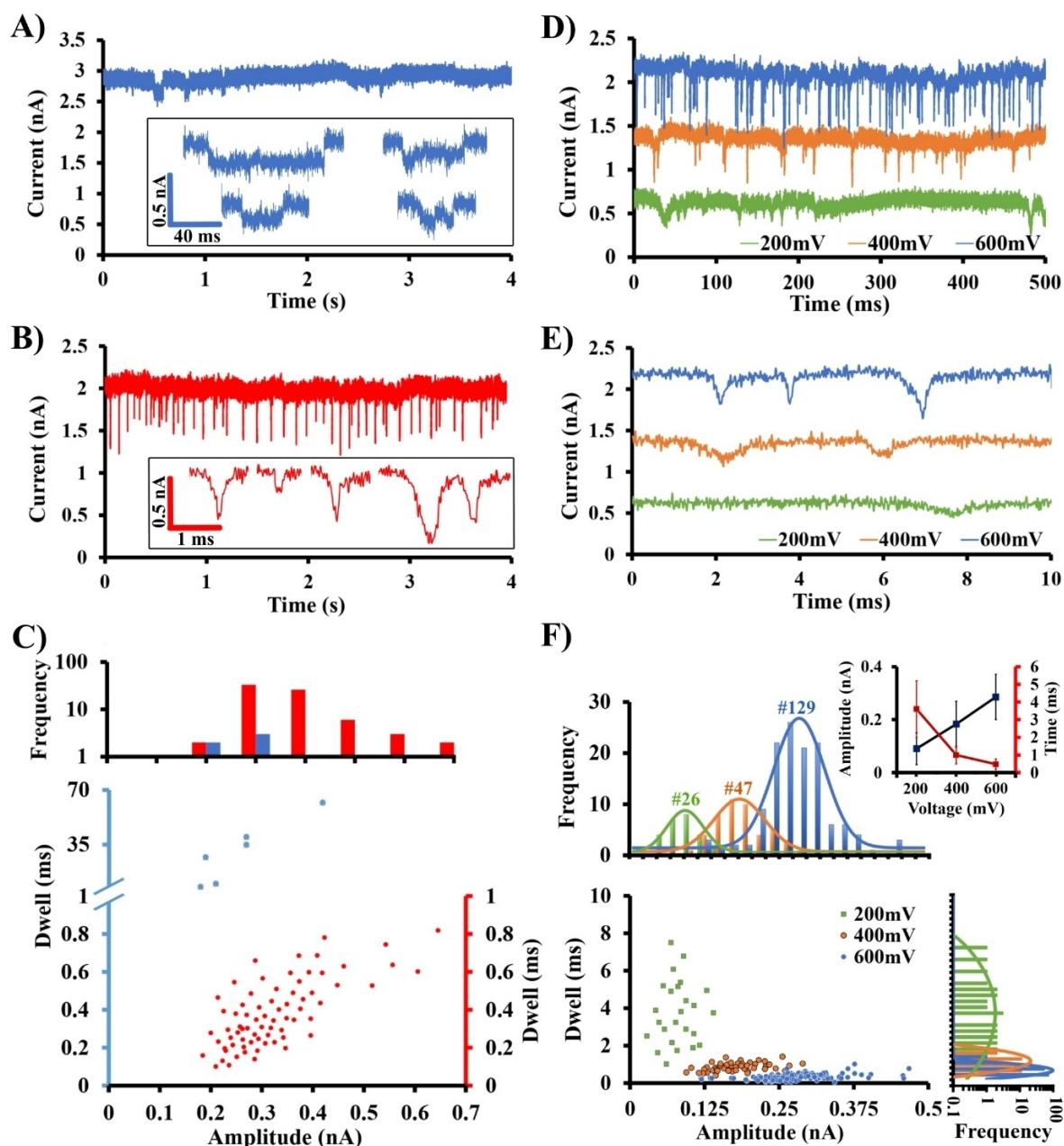


**Figure 4.** (A) 25 nM AAT protein translocation through 20 nm non-functionalized and (B) PLL-g-PEG functionalized SiN nanopores (30 nm thick) and (C) their Scatter plots of dwell time vs. blockade amplitude, and current blockade events histogram, represent the vertical (Dwell) axis scale change in the scatter plot of protein translocation through un-functionalized nanopore. Comparison of 500 nM AAT protein translocation events under different stimulus voltages (200, 400, and 600 mV) (D) during 500 ms and (E) 10 ms measurements. (F) 500 nM AAT translocation Events scatter plot of current blockage vs. translocation time in different voltages, the inset displays the events dwell time and amplitude changes with stimulus voltage based on the fitted Gaussian distribution curves with variance  $\sigma^2$ , and the # represent the total number of translocations events in each stimulus voltages. All measurements were done by using 1.0×PBS at physiological pH.

enhanced by increasing the voltage as demonstrates in Figure 4(F), the events number for 200, 400, and 600 mV are 26, 47, and 129 respectively. All these observations are in line with the previous research.<sup>[89–93]</sup>

AAT protein as one of the important globulin proteins in serum, has a 46 kDa with a density of 1.02 gr/cm<sup>3</sup> at 300 K.<sup>[94,95]</sup> Its volume can be calculated to be 74.9 nm<sup>3</sup>, by concerning its 46 kDa and using mass to density ratio ( $V=M/d$ ), however by using 60 kDa as SDS-PAGE MW for AAT protein, the estimated

volume would be around 97.7 nm<sup>3</sup>. On the other hand, AAT protein structural features such as those with length (7–8 nm) and width (4–5 nm) could be estimated by applying its crystal model which was introduced by Maria Gaczynska et al.<sup>[96]</sup> A volume of 231 nm<sup>3</sup> was reported by J. K. Armstrong assuming a 3.81 nm AAT protein hydrodynamic radius.<sup>[97]</sup> Since the methods used for the crystal structure-based volume and the experimental one was based on different principles and some parameters such as water shells weren't incorporated, such a

discrepancy was expected. The PLL-g-PEG functionalized nanopores allow us to estimate AAT molecular volume. As protein with volume  $\Delta$  is translocated through a pore with diameter of  $d$  and effective thickness of  $h_{\text{eff}}$ , the conductance blockade ( $\Delta G$ ) can be calculated from previous reports as follows:<sup>[98,99]</sup>

$$\Delta G = \frac{\sigma\gamma\Delta}{(h_{\text{eff}} + 0.8d)^2} S(d, a) \quad (3)$$

The 1.0×PBS buffer at 25°C has 1.6 (S/m) electrolyte solution conductivity. Based on DeBlois and Bean,<sup>[100]</sup> the correction factor  $S(d, a)$  depends on  $d$  and  $a$ , can be insignificant and close to one,<sup>[101]</sup> if the protein diameter ( $d_m$ ) is smaller than the estimated nanopore diameter,<sup>[97]</sup> and the length of fully folded AAT can be smaller than the effective length of the nanopore ( $l_m < h_{\text{eff}}$ ). On the other hand, the orientation of the AAT protein can affect the shape factor ( $\gamma$ ). Where  $\gamma$  is the electrical shape factor of 1.5 for a spherical molecule<sup>[102]</sup> and should result in normal distributions of  $\Delta I$  values.<sup>[103]</sup>

The conductance blockage vs dwell time of AAT protein translocations is depicted as a scatter plot in Figure 4(F) under different voltages. The average  $\Delta G$  for a single AAT protein is about  $\sim 0.43$  nS when the average current blockade under 600 mV stimulus voltage is  $\sim 0.26$  nA and the background current level of 2.2 nA is concerned. Therefore, the calculated volume and hydrodynamic radii of AAT protein at pH 7.4 are 253 nm<sup>3</sup> and 3.92 nm, respectively, which is close to the AAT volume reported by J.K. Armstrong (231 nm<sup>3</sup>).<sup>[97]</sup> The hydration shell thickness, surrounding water molecules, and counterions bind to the proteins more tightly, which may explain the difference between measured and estimated volumes (density ratio).<sup>[104,105]</sup>

## Conclusions

A miniaturized, leak-free, easy-to-assemble, and portable nanopore flowcell was designed and fabricated. We demonstrated that by decreasing buffer salt concentration from 1.0×PBS to 0.125×PBS, the ion current rectification ratio was changed from around 1 to 1.25 in a 20 nm SiN nanopore with 30 nm thickness. PLL-g-PEG polymer chains could easily self-assembled into the SiN nanopore's tip to prevent stickiness and interaction between the AAT protein with the SiN sidewall nanopore. Increasing stimulus voltage led to increases in the current rms noise level, however, the polarity of stimulus voltage affected the current noise level (when the base side of nanopore is positive, the noise level was 4 times lower than its negative polarity). *In situ* functionalization of PLL-g-PEG nanopores increased the continuous measurement time (nanopore life-time) up to four hours without any significant change in nanopore conductance, compared to non-functionalized SiN nanopores. *In situ* PLL-g-PEG functionalized SiN nanopore can be stored in 1.0×PBS at pH 7.4, for 5 times (each for 6 hours). The monitorable and real-time *in situ* functionalizing of PLL-g-PEG nanopore's tip surface has been proposed and developed

to translocate the non-sticky single AAT protein through solid-state nanopores. In addition, the amplitude of AAT protein translocation events was enhanced, also the decline in the dwell time and significantly increase in the number of translocation events were observed compared to the non-functionalized nanopore. In particular, the capability of the PLL-g-PEG functionalized nanopore to characterize single protein molecules was demonstrated, and the molecular volume of 253 nm<sup>3</sup> was measured for the AAT protein. This *in situ* functionalizing method can be used more efficiently and universally to characterize any type of nanoscale particles and biomolecules.

## Materials and methods

### Materials

Norcada (Canada) supplied 20 nm SiN nanopore chips with a 30 nm thick SiN layer. Phosphate-buffered saline (PBS) tablets, Methanol (MeOH), Sodium hypochlorite (NaOCl), Sulfuric acid 96% ultrapure (H<sub>2</sub>SO<sub>4</sub>), Calcium chloride (CaCl<sub>2</sub>), Sodium chloride (NaCl), Tris, Isopropanol (IPA), and Hydrogen peroxide (H<sub>2</sub>O<sub>2</sub>) were supplied by Sigma Aldrich. SuSoS AG provided PLL(20)-g[3.5]-PEG(2) (poly(l-lysine)-g-poly(ethylene glycol)). Eprelia™ coverslips were purchased from Fisher Scientific (#1.5). Fastscan-B AFM probes were acquired from Bruker. A recombinant Human Serpin A1/alpha-1-Antitrypsin Protein was purchased from Bio-Techne.

### Nanopore preparation

A schematic diagram of 20 nm solid-state nanopore chips with two window sizes of 10×10 μm and 250×250 μm are illustrated in Figure 1(c1). The flowcell frame consists of two Poly (methyl methacrylate) (PMMA) pieces. Nanopore chips were immersed in Piranha solution (1:3 mixture of H<sub>2</sub>O<sub>2</sub> and H<sub>2</sub>SO<sub>4</sub>) for 5 minutes, washed with deionized water, followed by drying at 60°C for 5 minutes to remove contaminants. As presented in Figure 1(A), the nanopore chips were sandwiched between two gaskets to prevent liquid leakage between PMMA chambers and compacted together with a white ring. As a result of the gaskets being completely stuck to the nanopore chip and completely isolating the two chambers from each other, there was no buffer solution leakage between the two chambers, so no current leakage was observed (extremely high current level) during all the experiments.

### Wetting the nanopore

To completely wet the nanopore, both chambers were fully filled with mixture of IPA and water (1:1 in volume) for 15 minutes. After each 5 minutes the mixture solution was gently replaced with fresh one, and at the end by injecting pure water for 5 times the alcohol was removed completely.



### Pseudo-reference electrodes preparation

The pseudo-reference electrodes were made by immersing the silver wires in 50% NaOCl for 2 minutes to chlorinate the Ag wires and dry them at room temperature.

### Nanopore operation and experiments

The time-resolved current measurement under constant voltage (V) was done using Nanopore reader from Elements Srl. The data acquisition was performed using Elements data reader (EDR) software (Elements srl, Italy), and all current traces were recorded at 100 kHz. The current blockades were detected by using EDR software feature "Event detection". The nanopore chips was first immersed in the Piranha solution and then washed with deionized water as explained above in "Nanopore preparation" section. Flowcells with a size of 1.6×1.6×0.8 cm are mounted on a printed circuit board (PCB) designed to facilitate the connection of terminals to a current measurement device to start nanopore experiments as illustrated in Figure 1(B). The quasi-references were then connected to the PCB terminals and placed in flowcell chambers and IPA solution was introduced into the chambers for 15 minutes, followed by deionized water injection, as explained above. Finally, the buffer solution injected into both chambers and the flow cell was inserted inside to nanopore reader.

During all ionic current measurements, the base side of nanopore chamber was connected to the ground electrode of the amplifier and the electrode of the nanopore's tip side chamber was connected to the working electrode of amplifier. Each nanopore chip was soaked for 5 minutes in water, ethanol, and chloroform following each experiment. When chips were not being used, they were stored in chloroform.

### Nanopore in-situ functionalization

PLL-g-PEG was diluted in 1.0×PBS to 0.01 mg/mL and stored at 5°C. The nanopore functionalization was performed by applying 800 mV stimulus voltage and adding 37 μL of PLL-g-PEG solution (directly into the nanopore's tip side chamber containing 1.0×PBS at pH 7.4 as depicted in Figure 1(c2). The tip side and base side of the nanopore chamber is filled with buffer containing PLL-g-PEG, and pure 1.0×PBS, respectively. Electrostatically binding of the PLL-g-PEG to the sidewall performs *in situ* functionalizing of the nanopore during their translocation. The structure and dimensions of the nanopore chip are shown in Figure 1(c1). The *in situ* PLL-g-PEG functionalization approach is shown in Figure 1(c2). A schematic image of protein translocation through functionalized PLL-g-PEG nanopore is illustrated in Figure 1(c3). For the ex-situ coating, the nanopores were deep coated in 1×PBS buffer containing 0.1 mg/mL PLL-g-PEG for 20 minutes.

### Protein samples preparation

Recombinant Human Serpin A1/alpha-1-Antitrypsin proteins were reconstituted at 100 μg/mL in sterile 50 mM Tris, 10 mM CaCl<sub>2</sub>, and 150 mM NaCl at pH 7.4. After diluting to 1 μg/mL, the protein solution was maintained at -20°C for further use. Before the protein translocation experiment, the chamber was rinsed three times with 1.0×PBS to remove the residual and non-interacted PLL-g-PEG chains.

### Nanopore and PLL-g-PEG lifetime characterization

The non-functionalized and *in situ* PLL-g-PEG functionalized 20 nm SiN nanopores over 10 times was stored (each storage time 6 hours) in 1.0×PBS at pH 7.4. The nanopore chips were immersed in 0.1×PBS for 6 hours, then washed for five minutes with DI water before and after I-V measurements to remove any PBS or other contaminants and dried by nitrogen gas between each storage process. To prevent buffer evaporation during storage, the entire chamber was sealed with parafilm.

### AFM imaging and lithography sample preparation

The thickness and uniformity of PLL-g-PEG functionalized on glass coverslips were determined using AFM. Glass coverslips were rinsed in 99% ethanol and glow discharged (25 mA, 45 seconds) before being placed with the glow discharged side of the coverslip facing a droplet (50 μL) of PLL-g-PEG (0.1 mg/mL in 1×PBS) on parafilm for 30 minutes. It was subsequently washed profusely in Milli-Q water and blow-dried with N<sub>2</sub>. AFM imaging of the PLL-g-PEG functionalized coverslip was performed in 1×PBS buffer using a Dimension Fastscan AFM (Bruker, USA) in PeakForce Quantitative Nanomechanical Mapping (QNM) mode, with a scan rate of 1.5 Hz, 256 lines and a PeakForce setpoint of 1 nN. For AFM lithography, the scanning mode was switched to contact mode and the surface scraped with the AFM tip using a scan size of 1 μm, a fast scan rate of 68 Hz and varying setpoints and times up to 9.5 V and 10 minutes, reaching a saturated depth where no more PLL-g-PEG could be scraped off. Imaging of the lithographic patterns was performed by switching back to QNM mode, using the aforementioned settings. Both imaging and lithography were performed with a Fastscan-B probe (nominal spring constant: 4 N. Final AFM images were analyzed using Nanoscope Analysis software (Bruker, USA) by flattening the images and measuring cross sections of the scraped squares.

### Acknowledgements

*This project has received funding from the Marie Skłodowska-Curie MSCA-ITN Single-Entity Nanoelectrochemistry, Sentinel [812398], Marie Skłodowska-Curie grant agreement ENSIGN-No.101086226, and also Independent Research Fund Denmark and Sino-Danish Center for Education and Research.*

## Conflict of Interests

The authors declare no conflict of interest.

## Data Availability Statement

The data that support the findings of this study are openly available in Mendeley Data at <https://doi.org/10.17632/36swjjrktm.1>, reference number 17632.

**Keywords:** Nanopore · Flowcell · In situ functionalization · Non-sticky · Protein

- [1] J. J. Kasianowicz, E. Brandin, D. Branton, D. W. Deamer, *Proc. Natl. Acad. Sci. USA* **1996**, *93*, 13770–13773.
- [2] D. Wendell, P. Jing, J. Geng, V. Subramaniam, T. J. Lee, C. Montemagno, P. Guo, *Nat. Nanotechnol.* **2009**, *4*, 765–772.
- [3] D. Fologea, M. Gershow, B. Ledden, D. S. McNabb, J. A. Golovchenko, J. Li, *Nano Lett.* **2005**, *5*, 1905–1909.
- [4] J. Li, M. Gershow, D. Stein, E. Brandin, J. A. Golovchenko, *Nat. Mater.* **2003**, *2*, 611–615.
- [5] D. W. Deamer, D. Branton, *Acc. Chem. Res.* **2002**, *35*, 817–825.
- [6] A. Han, G. Schürmann, G. Mondin, R. A. Bitterli, N. G. Hegelbach, N. F. De Rooij, U. Staufer, *Appl. Phys. Lett.* **2006**, *88*, 093901.
- [7] E. C. Yusko, P. Prangki, D. Sept, R. C. Rollings, J. Li, M. Mayer, *ACS Nano* **2012**, *6*, 5909–5919.
- [8] R. Hu, J. Diao, J. Li, Z. Tang, X. Li, J. Leitz, J. Long, J. Liu, D. Yu, Q. Zhao, *Sci. Rep.* **2016** *6*(1), 1–11.
- [9] K. Chuah, Y. Wu, S. R. C. Vivekchand, K. Gaus, P. J. Reece, A. P. Micolich, J. J. Gooding, *Nat. Commun.* **2019**, *10*, 1–9.
- [10] G. V. Soni, C. Dekker, *Nano Lett.* **2012**, *12*, 3180–3186.
- [11] J. Li, D. Stein, C. McMullan, D. Branton, M. J. Aziz, J. A. Golovchenko, *Nature* **2001**, *412*(6843), 166–169.
- [12] J. J. Kasianowicz, E. Brandin, D. Branton, D. W. Deamer, *Proc. Natl. Acad. Sci. USA* **1996**, *93*, 13770–13773.
- [13] M. M. Mohammadi, O. Bavi, *Biophys. Rev. Lett.* **2021**, *14*, 99–110.
- [14] N. A. W. Bell, K. Chen, S. Ghosal, M. Ricci, U. F. Keyser, *Nat. Commun.* **2017**, *8*, 1–8.
- [15] T. J. Morin, T. Shropshire, X. Liu, K. Briggs, C. Huynh, V. Tabard-Cossa, H. Wang, W. B. Dunbar, *PLoS One* **2016**, *11*, e0154426.
- [16] E. Atas, A. Singer, A. Meller, *Electrophoresis* **2012**, *33*, 3437–3447.
- [17] V. Tabard-Cossa, M. Wiggin, D. Trivedi, N. N. Jetha, J. R. Dwyer, A. Marziali, *ACS Nano* **2009**, *3*, 3009–3014.
- [18] E. C. Yusko, B. R. Bruhn, O. M. Eggenberger, J. Houghtaling, R. C. Rollings, N. C. Walsh, S. Nandivada, M. Pindrus, A. R. Hall, D. Sept, J. Li, D. S. Kalonia, M. Mayer, *Nat. Nanotechnol.* **2016**, *12*, 360–367.
- [19] K. Briggs, H. Kwok, V. Tabard-Cossa, *Small* **2014**, *10*, 2077–2086.
- [20] PLL(20)-g[3.5]-PEG(2), can be found under <https://susos.com/shop/pll20-g3-5-peg2/>, n.d.
- [21] X. Li, Y. Wang, F. Sun, Z. Cai, Y. Zhang, Q. Liu, *Proceedings – 2010 3rd International Conference on Biomedical Engineering and Informatics, BMEI 2010* **2010**, *4*, 1607–1609.
- [22] G. D. Sulka, S. Stroobants, V. Moshchalkov, G. Borghs, J.-P. Celis, *J. Electrochem. Soc.* **2002**, *149*, D97.
- [23] A. Crnković, M. Srnko, G. Anderluh, *Life* **2021**, *11*, 27.
- [24] J. Saharia, Y. M. N. D. Y. Bandara, B. I. Karawdeniya, J. R. Dwyer, M. J. Kim, *Small* **2023**, 2300198.
- [25] M. O'Donohue, J. Saharia, N. Bandara, G. Alexandrakis, M. J. Kim, *Electrophoresis* **2023**, *44*, 349–359.
- [26] M. C. Acharjee, H. Li, R. Rollings, B. Ma, S. Tung, J. Li, *J. Appl. Phys.* **2023**, *133*, 24701.
- [27] D. W. Cox, *Brenner's Encyclopedia of Genetics: Second Edition* **2013**, 85–87.
- [28] I. Blanco, *Blanco's Overview of Alpha-1 Antitrypsin Deficiency* **2017**, 23–37.
- [29] M. Higashiyama, O. Doi, K. Kodama, H. Yokouchi, R. Tateishi, *Br. J. Cancer* **1992**, *65*, 300–302.
- [30] Z. El-Akawi, Z. J. El-Akawi, A. M. Abu-Awad, N. A. Khouri, *World J. Oncol.* **2013**, *4*, 83–86.
- [31] G. Zhu, H. J. Lee, *Biosens. Bioelectron.* **2017**, *89*, 959–963.
- [32] Z. El-Akawi, A. Abu-Awad, A. Sharara, Y. Khader, *Neuroendocrinol. Lett.* **2010**.
- [33] Z. J. El-Akawi, F. K. Al-Hindawi, N. A. Bashir, *Neuroendocrinol. Lett.* **2008**, *29*, 482–484.
- [34] S. Solakidi, A. Dessypris, G. P. Stathopoulos, G. Androulakis, C. E. Sekeris, *Clin. Biochem.* **2004**, *37*, 56–60.
- [35] Y. Tournas, L. Sparos, C. H. Theodoropoulos, D. Trichopoulos, *Digestion* **1985**, *31*, 37–40.
- [36] B. Krishnan, L. M. Gierasch, *Nat. Struct. Mol. Biol.* **2011**, *18*(2), 222–226.
- [37] Y. Lu, L. R. Wang, J. Lee, N. S. Mohammad, A. M. Aranyos, C. Gould, N. Khodayari, R. A. Oshins, C. G. Moneypenny, M. L. Brantly, *Hepatol. Commun.* **2022**, *6*, 2354–2367.
- [38] E. Karatas, M. Boucheareilh, *Int. J. Mol. Sci.* **2020**, *21*, 1493.
- [39] G. H. Zerze, R. B. Best, J. Mittal, *J. Phys. Chem. B* **2015**, *119*, 14622–14630.
- [40] S. Awasthi, P. Sriboonpeng, C. Ying, J. Houghtaling, I. Shorubalko, S. Marion, S. J. Davis, L. Sola, M. Chiari, A. Radenovic, M. Mayer, *Small Methods* **2020**, *4*, 2000177.
- [41] D. J. Niedzwiecki, L. Moveleanu, *J. Visualization* **2011**, *58*, DOI 10.3791/3560.
- [42] O. M. Eggenberger, C. Ying, M. Mayer, *Nanoscale* **2019**, *11*, 19636–19657.
- [43] S. Acharya, A. Jiang, C. Kuo, R. Nazarian, K. Li, A. Ma, B. Siegal, C. Toh, J. J. Schmidt, *ACS Sens.* **2020**, *5*, 370–376.
- [44] Y. Wu, Y. Yao, S. Cheong, R. D. Tilley, J. J. Gooding, *Chem. Sci.* **2020**, *11*, 12570–12579.
- [45] X. Lei, J. Zhang, H. Hong, Z. Yuan, Z. Liu, *Micromachines (Basel)* **2022**, *13*, 923.
- [46] J. Nilsson, J. R. I. Lee, T. V. Ratto, S. E. Létant, *Adv. Mater.* **2006**, *18*, 427–431.
- [47] B. Malekian, R. L. Schoch, T. Robson, G. Ferrand-Drake del Castillo, K. Xiong, G. Emilsson, L. E. Kapinos, R. Y. H. Lim, A. Dahlin, *Front. Chem.* **2018**, *6*, 637.
- [48] J. R. Wayment, J. M. Harris, *Anal. Chem.* **2009**, *81*, 336–342.
- [49] Z. Siwy, L. Trofin, P. Kohli, L. A. Baker, C. Trautmann, C. R. Martin, *J. Am. Chem. Soc.* **2005**, *127*, 5000–5001.
- [50] M. Wanunu, A. Meller, *Nano Lett.* **2007**, *7*, 1580–1585.
- [51] B. N. Anderson, M. Muthukumar, A. Meller, *ACS Nano* **2013**, *7*, 1408–1414.
- [52] L. T. Sexton, H. Mukaibo, P. Katira, H. Hess, S. A. Sherrill, L. P. Horne, C. R. Martin, *J. Am. Chem. Soc.* **2010**, *132*, 6755–6763.
- [53] Z. Tang, B. Lu, Q. Zhao, J. Wang, K. Luo, D. Yu, *Small* **2014**, *10*, 4332–4339.
- [54] G. Emilsson, K. Xiong, Y. Sakiyama, B. Malekian, V. A. Gagnér, R. L. Schoch, R. Y. H. Lim, A. B. Dahlin, *Nanoscale* **2018**, *10*, 4663–4669.
- [55] G. F. Schneider, Q. Xu, S. Hage, S. Luik, J. N. H. Spoor, S. Malladi, H. Zandbergen, C. Dekker, *Nat. Commun.* **2013**, *4*, 1–7.
- [56] S. Awasthi, P. Sriboonpeng, C. Ying, J. Houghtaling, I. Shorubalko, S. Marion, S. J. Davis, L. Sola, M. Chiari, A. Radenovic, M. Mayer, *Small Methods* **2020**, *4*, 2000177.
- [57] M. Lepoitevin, B. Jamilloux, M. Bechelany, E. Balanzat, J. M. Janot, S. Balme, *RSC Adv.* **2016**, *6*, 32228–32233.
- [58] Z. Tang, B. Lu, Q. Zhao, J. Wang, K. Luo, D. Yu, *Small* **2014**, *10*, 4332–4339.
- [59] R. Michel, S. Pasche, M. Textor, D. G. Castner, *Langmuir* **2005**, *21*, 12327.
- [60] R. Marie, J. P. Beech, J. Vörös, J. O. Tegenfeldt, F. Höök, *Langmuir* **2006**, *22*, 10103–10108.
- [61] R. Marie, J. P. Beech, J. Vörös, J. O. Tegenfeldt, F. Höök, *Langmuir* **2006**, *22*, 10103–10108.
- [62] S. W. Kowalczyk, A. Y. Grosberg, Y. Rabin, C. Dekker, *Nanotechnology* **2011**, *22*, 315101.
- [63] L. Ma, Z. Li, Z. Yuan, C. Huang, Z. S. Siwy, Y. Qiu, *Anal. Chem.* **2020**, *92*, 16188–16196.
- [64] L. Jubin, A. Poggioli, A. Siria, L. Bocquet, *Proc. Natl. Acad. Sci. USA* **2018**, *115*, 4063–4068.
- [65] W. Cao, J. Wang, M. Ma, W. Sparreboom, A. Van Den Berg, J. C. T. Eijkel, *New J. Phys.* **2010**, *12*, 015004.
- [66] M. Trivedi, N. Nirmalkar, *Sci. Rep.* **2022**, *12*, 1–16.
- [67] M. Wanunu, T. Dadosh, V. Ray, J. Jin, L. McReynolds, M. Drndić, *Nat. Nanotechnol.* **2010**, *5*, 807–814.

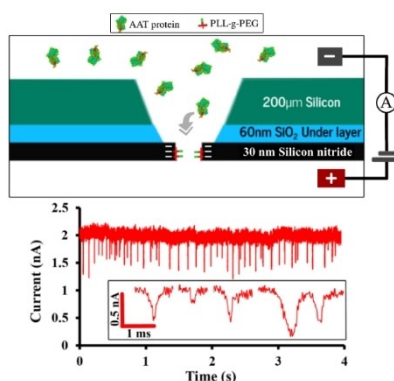
- [68] L. Ma, Z. Li, Z. Yuan, C. Huang, Z. S. Siwy, Y. Qiu, *Anal. Chem.* **2020**, *92*, 16188–16196.
- [69] Y. Wang, Q. Chen, T. Deng, Z. Liu, *J. Phys. Chem. C* **2018**, *122*, 11516–11523.
- [70] S. Zeng, C. Wen, P. Solomon, S. L. Zhang, Z. Zhang, *Nat. Nanotechnol.* **2019**, *14*, 1056–1062.
- [71] Y. Zhang, G. C. Schatz, *J. Phys. Chem. C* **2017**, *121*, 161–168.
- [72] A. Vacic, J. M. Criscione, N. K. Rajan, E. Stern, T. M. Fahmy, M. A. Reed, *J. Am. Chem. Soc.* **2011**, *133*, 13886–13889.
- [73] C. H. Chu, I. Sarangadharan, A. Regmi, Y. W. Chen, C. P. Hsu, W. H. Chang, G. Y. Lee, J. I. Chyi, C. C. Chen, S. C. Shiesh, G. Bin Lee, Y. L. Wang, *Sci. Rep.* **2017**, *7*, 1–15.
- [74] E. Mádai, B. Matejczyk, A. Dallos, M. Valiskó, D. Boda, *Phys. Chem. Chem. Phys.* **2018**, *20*, 24156–24167.
- [75] T. Gamble, K. Decker, T. S. Plett, M. Pevarnik, J. F. Pietschmann, I. Vlasiouk, A. Aksimentiev, Z. S. Siwy, *J. Phys. Chem. C* **2014**, *118*, 9809–9819.
- [76] L. H. Yeh, M. Zhang, N. Hu, S. W. Joo, S. Qian, J. P. Hsu, *Nanoscale* **2012**, *4*, 5169–5177.
- [77] K. Lin, Z. Li, Y. Tao, K. Li, H. Yang, J. Ma, T. Li, J. Sha, Y. Chen, *Langmuir* **2021**, *37*, 10521–10528.
- [78] B. I. Karawdeniya, Y. M. N. D. Y. Bandara, J. W. Nichols, R. B. Chevalier, J. R. Dwyer, *Nat. Commun.* **2018**, *9*, 1–8.
- [79] B. N. Anderson, M. Muthukumar, A. Meller, *ACS Nano* **2013**, *7*, 1408–1414.
- [80] R. Schlapak, D. Armitage, N. Saucedo-Zeni, W. Chrzanowski, M. Hohage, D. Caruana, S. Howorka, *Soft Matter* **2009**, *5*, 613–621.
- [81] L. Ionov, A. Synytska, E. Kaul, S. Diez, *Biomacromolecules* **2010**, *11*, 233–237.
- [82] T. Ron, J. B. Madsen, N. Nikorgeorgos, S. Lee, *Tribol. Lubr.* **2014**, *30*, 247–255.
- [83] Y. He, D. Gillespie, D. Boda, I. Vlasiouk, R. S. Eisenberg, Z. S. Siwy, *J. Am. Chem. Soc.* **2009**, *131*, 5194–5202.
- [84] J. Cervera, B. Schiedt, R. Neumann, S. Mafá, P. Ramírez, *J. Chem. Phys.* **2006**, *124*, 104706.
- [85] R. M. M. Smeets, U. F. Keyser, M. Y. Wu, N. H. Dekker, C. Dekker, *Phys. Rev. Lett.* **2006**, *97*, 088101.
- [86] Z. Siwy, A. Fuliński, *Phys. Rev. Lett.* **2002**, *89*, 158101.
- [87] Q. Li, Q. Zhao, B. Lu, H. Zhang, S. Liu, Z. Tang, L. Qu, R. Zhu, J. Zhang, L. You, F. Yang, D. Yu, *Nanoscale* **2012**, *4*, 1572–1576.
- [88] Y. C. Chou, P. Masih Das, D. S. Monos, D. S. Monos, M. Drndić, *ACS Nano* **2020**, *14*, 6715–6728.
- [89] A. Oukhaled, B. Cressiot, L. Bacri, M. Pastoriza-Gallego, J. M. Betton, E. Bourhis, R. Jede, J. Gierak, L. Auvray, J. Pelta, *ACS Nano* **2011**, *5*, 3628–3638.
- [90] E. Angeli, A. Volpe, P. Fanzio, L. Repetto, G. Firpo, P. Guida, R. Lo Savio, M. Wanunu, U. Valbusa, *Nano Lett.* **2015**, *15*, 5696–5701.
- [91] Q. Liu, H. Wu, L. Wu, X. Xie, J. Kong, X. Ye, L. Liu, *PLoS One* **2012**, *7*, e46014.
- [92] L. Restrepo-Pérez, S. John, A. Aksimentiev, C. Joo, C. Dekker, *Nanoscale* **2017**, *9*, 11685–11693.
- [93] N. Varongchayakul, J. Song, A. Meller, M. W. Grinstaff, *Chem. Soc. Rev.* **2018**, *47*, 8512.
- [94] P. Y. Berclaz, B. C. Trapnell, *Kendig's Disorders of the Respiratory Tract in Children* **2006**, 747–761.
- [95] E. D. Sangachini, S. Hasannia, M. Taghdir, N. Pirooznia, K. K. Ghadicholaei, *Electron. J. Biotech.* **2012**, *15*, 94–103.
- [96] M. Gaczynska, P. Karpowicz, C. E. Stuart, M. G. Norton, J. H. Teckman, E. Marszal, P. A. Osmulski, *PLoS One* **2016**, *11*, e0151902.
- [97] J. K. Armstrong, R. B. Wenby, H. J. Meiselman, T. C. Fisher, *Biophys. J.* **2004**, *87*, 4259–4270.
- [98] L. J. Steinbock, S. Krishnan, R. D. Bulushev, S. Borgeaud, M. Blokesch, L. Feletti, A. Radenovic, *undefined* **2014**, *6*, 14380–14387.
- [99] N. B. Grover, J. Naaman, S. Ben-Sasson, F. Doljanski, *Biophys. J.* **1972**, *12*, 1099–1117.
- [100] R. W. DeBlois, C. P. Bean, *Rev. Sci. Instrum.* **2003**, *41*, 909.
- [101] B. Ledden, D. Fologea, D. S. Talaga, J. Li, J. Li, S. M. Iqbal, R. Bashir, *Nanopores* **2011**, 129–150.
- [102] A. Carlsen, V. Tabard-Cossa, *Proteomics* **2022**, *22*, 2100068.
- [103] E. C. Yusko, B. R. Bruhn, O. M. Eggenberger, J. Houghtaling, R. C. Rollings, N. C. Walsh, S. Nandivada, M. Pindrus, A. R. Hall, D. Sept, J. Li, D. S. Kalonia, M. Mayer, *Nat. Nanotechnol.* **2016**, *12*, 360–367.
- [104] A. Balijepalli, J. W. F. Robertson, J. E. Reiner, J. J. Kasianowicz, R. W. Pastor, *J. Am. Chem. Soc.* **2013**, *135*, 7064–7072.
- [105] E. C. Yusko, R. An, M. Mayer, *ACS Nano* **2010**, *4*, 477–487.

---

Manuscript received: June 9, 2023  
 Revised manuscript received: July 3, 2023  
 Version of record online: ■■, ■■

## RESEARCH ARTICLE

**In-situ functionalization** of thin PLL-g-PEG on SiN nanopores based on the self-assembly and electrostatic interaction between the nanopore and PLL backbone of PLL-g-PEG is reported. This functionalization of SiN nanopores leads to non-sticky protein translocation and volume estimation of individual proteins. Most significantly, our in situ method is monitorable for direct evaluation of functionalization before non-sticky protein translocation.



*Dr. M. Salehrozveh, A.-K. Kure Larsen,  
Dr. M. Stojmenovic, Dr. F. Thei\*,  
Prof. M. Dong\**

1 – 12

**In-situ PLL-g-PEG Functionalized  
Nanopore for Enhancing Protein  
Characterization**

